



## RESEARCH LETTER

10.1002/2016GL068560

## Key Points:

- A 0.3–3% metallic melt can produce the features of the large low shear velocity provinces
- Trapping of metallic melt is likely during the crystallization of a dense basal magma ocean
- Large low shear velocity provinces can become a primordial geochemical mantle reservoir

## Supporting Information:

- Supporting Information S1

## Correspondence to:

Z. Zhang,  
zhan1721@umn.edu

## Citation:

Zhang, Z., S. M. Dorfman, J. Labidi, S. Zhang, M. Li, M. Manga, L. Stixrude, W. F. McDonough, and Q. Williams (2016), Primordial metallic melt in the deep mantle, *Geophys. Res. Lett.*, 43, 3693–3699, doi:10.1002/2016GL068560.

Received 7 MAR 2016

Accepted 29 MAR 2016

Accepted article online 5 APR 2016

Published online 25 APR 2016

Corrected 5 MAY 2016

This article was corrected on 5 MAY 2016.  
See the end of the full text for details.

The copyright line for this article was changed on 5 MAY 2016 after original online publication.

©2016. The Authors.

This is an open access article under the terms of the Creative Commons Attribution-NonCommercial-NoDerivs License, which permits use and distribution in any medium, provided the original work is properly cited, the use is non-commercial and no modifications or adaptations are made.

## Primordial metallic melt in the deep mantle

Zhou Zhang<sup>1</sup>, Susannah M. Dorfman<sup>2,3</sup>, Jabrane Labidi<sup>4</sup>, Shuai Zhang<sup>5</sup>, Mingming Li<sup>6,7</sup>, Michael Manga<sup>5</sup>, Lars Stixrude<sup>8</sup>, William F. McDonough<sup>9</sup>, and Quentin Williams<sup>10</sup>

<sup>1</sup>Department of Earth Sciences, University of Minnesota, Minneapolis, Minnesota, USA, <sup>2</sup>Earth and Planetary Science Laboratory, Ecole Polytechnique Fédérale de Lausanne, Lausanne, Switzerland, <sup>3</sup>Now at Department of Earth and Environmental Sciences, Michigan State University, East Lansing, Michigan, USA, <sup>4</sup>Geophysical Laboratory, Carnegie Institute of Washington, Washington, District Columbia, USA, <sup>5</sup>Department of Earth and Planetary Science, University of California, Berkeley, California, USA, <sup>6</sup>School of Earth and Space Exploration, Arizona State University, Tempe, Arizona, USA, <sup>7</sup>Now at Department of Physics, University of Colorado Boulder, Boulder, Colorado, USA, <sup>8</sup>Department of Earth Sciences, University College London, London, UK, <sup>9</sup>Department of Geology, University of Maryland, College Park, Maryland, USA, <sup>10</sup>Department of Earth and Planetary Sciences, University of California, Santa Cruz, California, USA

**Abstract** Seismic tomography models reveal two large low shear velocity provinces (LLSVPs) that identify large-scale variations in temperature and composition in the deep mantle. Other characteristics include elevated density, elevated bulk sound speed, and sharp boundaries. We show that properties of LLSVPs can be explained by the presence of small quantities (0.3–3%) of suspended, dense Fe-Ni-S liquid. Trapping of metallic liquid is demonstrated to be likely during the crystallization of a dense basal magma ocean, and retention of such melts is consistent with currently available experimental constraints. Calculated seismic velocities and densities of lower mantle material containing low-abundance metallic liquids match the observed LLSVP properties. Small quantities of metallic liquids trapped at depth provide a natural explanation for primitive noble gas signatures in plume-related magmas. Our model hence provides a mechanism for generating large-scale chemical heterogeneities in Earth's early history and makes clear predictions for future tests of our hypothesis.

## 1. Introduction

The origins of the two large low shear velocity provinces (LLSVPs) in the deep mantle beneath Africa and the central Pacific have been enigmatic and controversial since their discovery in seismic tomographic models [Su *et al.*, 1994; Li and Romanowicz, 1996]. These features are believed to play a key role in the convective circulation of the deep mantle [e.g., Davaille, 1999; McNamara and Zhong, 2005; Deschamps *et al.*, 2012]. The colocation of LLSVPs with reconstructed past hotspot locations over the last several hundred million years may account for the primordial geochemical signatures observed in hotspot lavas [Burke *et al.*, 2008; Torsvik *et al.*, 2010; Jackson and Carlson, 2011]. Indeed, geodynamic simulations show that large mantle structures can remain stable at the base of the mantle throughout Earth's history if they are denser than the surrounding mantle [Jellinek and Manga, 2002; McNamara and Zhong, 2005].

Observed characteristics of the LLSVPs, which extend from the core-mantle boundary to heights of 400–1000 km and with breadths on the scale of approximately thousands of kilometers, include depressed shear wave velocity (~3–4% relative to average mantle) [Garnero, 2000], elevated density (~1% relative to average mantle) [Ishii and Tromp, 1999], possibly elevated bulk sound speed, and sharp boundaries [Ni *et al.*, 2002]. Three scenarios might produce these seismic signatures: a temperature anomaly ~400–800 K hotter than surrounding mantle [Davies *et al.*, 2012]; a variation in major element composition, with modest enrichment in iron and silicon relative to an assumed pyrolytic composition [Deschamps *et al.*, 2012]; or a combination of thermal and chemical effects. Support for higher temperatures in LLSVPs relative to the surrounding mantle includes geodetic evidence for dynamic upwelling [McNutt, 1998] and geochemical evidence for plume volcanism above these regions [Burke *et al.*, 2008; Torsvik *et al.*, 2010]. Long-term stability of compositional heterogeneities at the base of the mantle implies that their chemical density, likely due to elevated iron content, exceeds their thermal buoyancy. The sharp boundaries of the LLSVPs and the anticorrelation between shear and bulk sound seismic velocities point to compositional differences [Su *et al.*, 1994], but a composition that matches geophysical observations and a corresponding process that forms large-scale heterogeneities of this composition have not been uniquely identified.

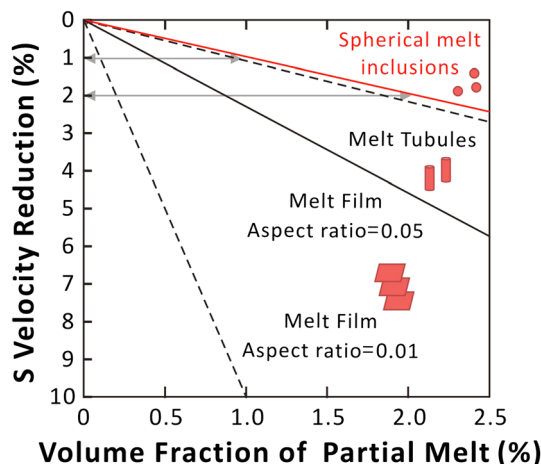


**Figure 1.** Effect of melt percentage and geometry on shear wave velocity reduction of bulk phase assemblage, based on parameters in the calculation from Williams and Garnero, [1996] (see supporting information Text S1 for details).

[Williams and Garnero, 1996] (Figure 1; see supporting information Text S1 for details). A molten phase in a potentially primordial, undegassed region would store ancient noble gases [Coltice et al., 2011]. The melting points of the major silicate and oxide phases of the lower mantle are, however, too high to permit widespread melting over the large scale of the anomalies (Figure 2 and see supporting information Text S2 for details). In contrast, a separate minor metallic Fe-Ni-S phase would be molten at LLSVP pressures and temperatures (Figure 2 and see supporting information Text S2 for details) and would increase the density of the bulk assemblage (the density of pure Fe alloy is about twice that of ambient silicate mantle). A suspension of small quantities (<3%) of Fe-Ni-S liquid within LLSVPs could thus explain their depressed shear velocities and their location at the base of the mantle. Here we present a process for generating partially molten, Fe-Ni-S liquid-bearing LLSVPs from the differentiation and cooling of the early Earth, and discuss its consistency with geochemical and geophysical constraints.

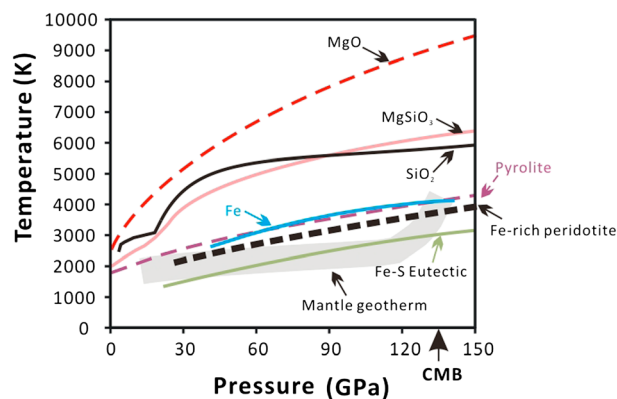


**Figure 2.** Pressure dependence of melting points of lower mantle components. MgO: Alfe [2005]; MgSiO<sub>3</sub>: Stixrude and Karki [2005]; SiO<sub>2</sub>: Usui and Tsuchiya [2010]; Pyrolite: Fiquet et al. [2010]; Fe: Anzellini et al. [2013]; Fe-S eutectic: Kamada et al. [2012]; and mantle geotherm: Stixrude et al. [2009]. Fe-rich peridotite: 400 K lower than pyrolite according to low-pressure (0–10 GPa) studies on the solidus of peridotite with Mg# 90 and Mg# 70 and the fayalite-forsterite binary [Hirschmann, 2000; Wasylenski et al., 2003]. CMB stands for core-mantle boundary.

A few mechanisms have been proposed for generating large-scale chemical heterogeneities early in Earth's history, through the enrichment of Fe, Si, and/or basaltic material [Christensen and Hofmann, 1994; Labrosse et al., 2007; Lee et al., 2010; Deschamps et al., 2012]. These models view Fe as sequestered within solid silicates in an oxidized form. Here we propose a new model that is focused on ancient portions of the mantle retaining small quantities of molten, Fe-Ni-S metallic blebs, in a manner analogous to that proposed in the mantle with low oxygen fugacity [Frost et al., 2004; Rohrbach et al., 2007]. Hence, our model differs fundamentally from prior models in its proposed redox state of iron.

## 2. Our Model

The slow shear wave speed that defines the LLSVPs and inferred elevated temperature are consistent with the presence of a small amount of melt information Text S1 for details). A molten phase in a

We propose that the crystallization of a basal magma ocean [Labrosse et al., 2007] incorporated inclusions of Fe-Ni-S liquid in a dense cumulate layer, which became the modern LLSVPs. Formation of metal through charge disproportionation of divalent iron represents a separate, complementary possibility for producing a metallic phase [Frost et al., 2004]. The metallic phase contributes to a compositional density anomaly of a few percent. Mantle convection simulations show that a dense basal layer with appropriate viscosity contrasts relative to ambient mantle will be advected into mounds with a pile-like morphology akin to that observed today [McNamara and Zhong, 2005; Davies et al., 2012].

## 3. Consistency With Geophysical Observations

Figure 1 shows the shear velocity depression resulting from small amounts of melt,

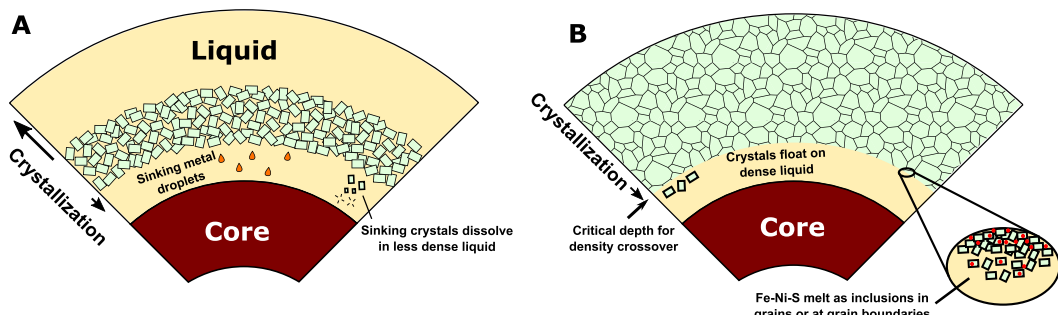


**Figure 3.** Magma ocean solidification. (a) Initiation of mantle crystallization and segregation of rapidly crystallizing upper magma ocean and slowly crystallizing basal magma ocean. (b) At the density crossover of crystallizing basal magma ocean, floating crystals trap Fe-Ni-S liquid.

based on the elasticity of two-phase aggregates (see supporting information Text S1 for details). The seismic velocity decrement associated with LLSVPs of  $\sim 2$  ( $\pm 1$ )% [Li and Romanowicz, 1996; Ishii and Tromp, 1999] can be generated by 0.3–3% of trapped iron-rich melt, with values at the low end of this range expected if metallic melt tends to wet grain boundaries [Shi *et al.*, 2013]. The presence of 1% pure Fe metal yields a chemical density contrast of  $\sim 1\%$ . The estimated density anomaly decreases with increasing light-element content in the Fe-Ni-S liquid and temperature difference relative to the surrounding mantle. For a given amount of iron alloy, and assuming a LLSVP 500 K hotter than its surroundings [Deschamps *et al.*, 2012], the density is further reduced by  $\sim 0.5\%$  due to thermal expansion and the shear velocity is further reduced by  $\delta \ln V_S \sim -1.5\%$  (see supporting information Text S3 for details). The total changes of shear velocity and density of LLSVPs caused by combined compositional and thermal effects are consistent with current models of seismic observations [Li and Romanowicz, 1996; Ishii and Tromp, 1999]. Other geophysical probes, such as electrical conductivity inversions and neutrino tomography, do not currently constrain the viability of our model due to a lack of spatial resolution in the current observational data set.

#### 4. Dynamic Process

Following the moon-forming impact, the mantle was totally molten [Nakajima and Stevenson, 2015]. The segregation of a primordial, dense layer at the base of the mantle may arise from crystallization of a magma ocean. Crystallization has been suggested to begin at midmantle pressures, where the adiabatic temperature profile of the cooling magma ocean intersects the liquidus of the bulk silicate Earth [Stixrude *et al.*, 2009], dividing the magma ocean into upper and deeper oceans (Figure 3a). The upper magma ocean will freeze within  $10^7$  years owing to rapid radiative and convective heat loss to the atmosphere [Hamano *et al.*, 2013]. The deeper magma ocean cools much more slowly, as heat loss is limited by solid-state convection in the overlying mantle, with a solidification time of  $10^9$  years [Labrosse *et al.*, 2007] (supporting information Text S4 for details).

During the early stages of deep magma ocean solidification, the precipitation of metal droplets could be driven by a decrease of sulfur solubility in silicate liquid due to cooling ("Hadean matte") [O'Neill, 1991] and / or Fe disproportionation through the reaction  $[3\text{Fe}^{2+} \text{ (magma)} \leftrightarrow 2\text{Fe}^{3+} \text{ (bridgmanite)} + \text{Fe}^0 \text{ (metallic melt)}]$  at oxygen fugacities near iron-wüstite-2 [Frost *et al.*, 2004]. Once Fe precipitates from the silicate liquid, Ni and light elements (such as S, C, and O) will concentrate in this phase. Assuming sulfur saturation in the silicate liquid ( $\sim 400 \mu\text{g/g}$ ) implies that the  $(\text{Fe} + \text{Ni})/\text{S}$  atomic ratio ranges from 3 to 100. The possible presence of other lighter alloying components (such as oxygen or carbon) within these is, however, neither mandated nor precluded (see supporting information Text S5 for details).

Both the crystals and Fe-Ni-S liquids that exsolve during crystallization are denser than the residual melt. Sinking crystals move to conditions above their melting points and should redissolve into the magma ocean. For metal droplets to settle to the core, they must be large enough to settle faster than the speeds of both the solidification front and the velocity fluctuations in the convecting magma ocean. Experimental observations suggest that exsolved metallic melt droplets initially have radii  $r_0 \sim 10^{-6} \text{ m}$ , giving an expected

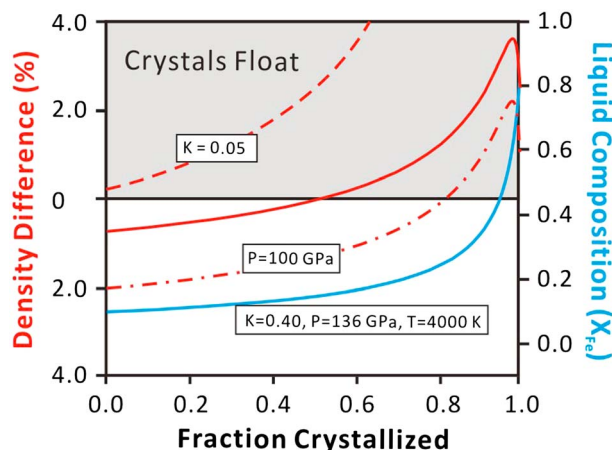


**Figure 4.** Melt composition and density evolution. Variation of the liquid-solid density contrast (bold red) and liquid composition (blue) at 136 GPa and 4000 K, assuming a value of the Mg-Fe solid-liquid partition coefficient  $K = 0.4$  [Andrault et al., 2012]. Also shown are the density contrasts computed for an alternate value of pressure (100 GPa) and partition coefficient ( $K = 0.05$ ) [Nomura et al., 2011]. The density of liquid and crystalline phases is computed following the method of Muñoz Ramo and Stixrude [2014] (see supporting information Text S9 for details). Metallic melt precipitation drives the density contrast curves left, reaching the crystal-liquid density crossover at shallower depth.

A density crossover in the magma ocean near the end of its solidification allows metallic melt droplets to be trapped within floating, crystallizing silicates (see supporting information Text S8 and Text S9 for details) (Figure 3b). At a critical depth that depends on composition and melt-silicate partitioning, the residual silicate melt becomes denser than the crystallizing phases (see supporting information Text S9 for details). With the crystallization of residual silicate melt, the bridgmanite and ferropericlase crystals are enriched in Fe compared with the bulk silicate Earth, increasing their bulk moduli and providing a possible explanation for the elevated bulk modulus of LLSPs (Figure 4). The buoyant crystals may then trap metal droplets formed at the solidification front at grain boundaries (see supporting information Text S8 for details). Laboratory experiments suggest that metal may wet bridgmanite at high pressure, allowing metal to drain [Shi et al., 2013]. Wetting behavior strongly depends on the sample environment [Walte et al., 2011; Ghanbarzadeh et al., 2015], and the role of nonhydrostatic experimental conditions in generating connectivity in bridgmanite-metal aggregates remains unclear. Within the pioneering experiments of Shi et al. [2013], a few percent of the metal remains as isolated droplets, and even wetting fluids are commonly trapped as fluid inclusions during crystal growth [Shaw and Duncombe, 1991]. Other factors such as low permeability and surface tension will generate a strong force resisting complete draining of small amount of liquid at solid silicate grain boundaries (see supporting information Text S8 for details) [Belien et al., 2010; Holtzman, 2016]. Experiments also suggest that deformation with silicate liquid present does not promote the drainage of the metal or sulfide component [Cerantola et al., 2015]. Thus, even if the bulk of the metallic component is lost, a small volume fraction of a few percent metallic melt may still remain trapped as isolated droplets, likely with high aspect ratios as in Shi et al. [2013]. Alternatively, if the magma ocean solidifies from the core-mantle boundary upward, exsolved metal will be trapped with the minerals that crystallize at or near the crystal-liquid interface: any deep crystal-liquid density crossover [Muñoz Ramo and Stixrude, 2014] will facilitate this trapping. Sharp boundaries separating metal-rich and metal-poor regions might then be associated with depth-varying changes in redox state.

settling rate of  $u_s \sim 10^{-8}$  m/s. Although  $u_s$  exceeds the speed at which the solidification front moves downward,  $10^{-10}$  m/s, it is small relative to convective velocities in the magma ocean,  $10^{-2}$  m/s, and the magnitude of velocity fluctuations at the Kolmogorov scale,  $10^{-4}$  m/s (see supporting information Text S6 for details). Droplets will coalesce as they sink under the influence of gravity and as they are brought into contact by flow in the convecting magma ocean. Droplets will grow to reach radii large enough that their settling speed exceeds the convective velocity over short time scales,  $10^3$  to  $10^6$  s (see supporting information Text S6 for details). Although both inertial forces and turbulent stress fluctuations will limit the maximum size of droplets to about  $10^{-3}$  to  $10^{-2}$  m, droplets of this size are still larger than the minimum required to sink to the core. Thus, at this stage, the crystallizing lower mantle is nearly free of metallic Fe-Ni-S liquids (see supporting information Text S7 for details).

## 5. Consistency With Geochemical Observations

The metallic melt droplets are Fe-Ni-S liquids, which might contain up to  $10^1$  to  $10^4$  higher concentrations of platinum group elements (PGEs) and Ni than ambient mantle (see supporting information Text S10 for

details). Because LLSVPs comprise  $10^{-2}$  to  $10^{-1}$  of the whole mantle, and the metallic melt is  $\sim 10^{-2}$  of the LLSVPs in our model, these abundances have small effects on the composition of hot spot magmas that might sample LLSVPs; accordingly, they also do not alter the global volatility trend of these elements within the bulk Earth (see supporting information Text S10 for details).

Our calculations thus suggest that the Fe-Ni-S liquid is not expected to create resolvable PGEs and Ni anomalies nor W isotope anomalies (see supporting information Text S10 for details). However, Fe-Ni-S liquid or silicate/oxide crystals in LLSVPs might contain primordial noble gas compositions with significant differences from ambient mantle. Despite being the most studied noble gas, little is known about helium partitioning between silicate solids/silicate melt or silicate solids/metallic melt under relevant lower mantle pressures and temperatures. Both Fe-Ni-S liquid and its adjacent silicate crystals are potential candidates noble gas carriers, depending on their noble gas solubility (Figure S2). On the one hand, if helium is preferentially partitioned into Fe-Ni-S liquid, the Fe-Ni-S liquid could potentially store significant primordial noble gases compared with silicate crystals [Heber *et al.*, 2007; Bouhifd *et al.*, 2013; Huang *et al.*, 2014]. On the other hand, if noble gases were to have higher silicate solid/liquid partition coefficients at high pressure (e.g., Xe: Sanloup *et al.* [2011]), they could be stored in silicate phases rather than Fe-Ni-S liquids. In this scenario, the droplet occurrence would only have acted as a physical mechanism to isolate the LLSVP from whole mantle convection (through a density increase) but not as the host of the noble gases (especially Xe). In both cases, the occurrence of the metallic droplets creates the geological context preservation of the primordial noble gas signatures in LLSVPs.

Mechanical entrainment by upwellings, from either the sides or top of the LLSVPs, provides the mechanism that delivers material containing primordial noble gas signatures from depth to hotspot-related surface volcanism. Furthermore, it is noteworthy that the reconstructed eruption of lavas that have high  ${}^3\text{He}/{}^4\text{He}$  ratios (as well as primordial Ne, Ar, and Xe isotope compositions) [Mukhopadhyay, 2012] lie close to, or within, the inferred boundaries of the African (for which low velocities extend substantially north beneath the Atlantic to near Icelandic latitudes) or Pacific LLVSPs [Lekic *et al.*, 2012; Rickers *et al.*, 2013].

## 6. Discussion

Recent compositional models of LLSVPs have proposed that a combination of iron and  $(\text{Mg},\text{Fe})\text{SiO}_3$ -bridgmanite enrichment (~3% and 18%, respectively) could explain their observed seismic velocity and density characteristics [Deschamps *et al.*, 2012]. However, how such compositions might be generated in the deep Earth remains enigmatic (see supporting information Text S11 for details). There is also the possibility that small amounts of silicate liquids might be present within LLSVPs [e.g., Lay *et al.*, 2004]. Such silicate liquids, however, would be expected to equilibrate with their coexisting solids, and current estimates of iron partitioning in natural assemblages coupled with inferred volumes of fusion indicate that such liquids would be generally similar in density to their coexisting solids [e.g., Andrault *et al.*, 2012]. Therefore, producing the apparently elevated density of LLSVP's via silicate melting would involve amounts of liquid that are incompatible with the observed shear wave velocities.

The metallic melt model, using a single compositional component that can arise through the simple mechanism of trapping and inefficient extraction of iron from portions of the mantle, quantitatively explains known LLSVP properties: the decrement of shear velocity, a small density increase (in accord with current seismic constraints), and sharp edges of these features. From a geochemical perspective, the presence of Fe-Ni-S liquid or adjacent silicate and oxide crystals in LLSVPs also provides a plausible location to store incompatible noble gases.

Our hypothesis can be tested by a combination of future geophysical observations and laboratory studies (see supporting information Text S12 for details). Specifically, the model makes a clear prediction for the relationship between density and seismic anomalies and implies locally increased electrical conductivity. Laboratory experiments can also provide tests of some of the features built into the evolutionary model for creating LLSVPs. Constraints that are needed are (1) noble gas partitioning experiments at  $\sim 100$  GPa to quantify partitioning between silicate crystals, metallic melt, and silicate melt; (2) experiments with silicate liquids with a range of compositions at lower mantle pressures, temperatures, and oxygen fugacity to quantify Fe-Ni-S liquid amount and composition; (3) an accurate oxygen fugacity depth profile in the magma ocean to constrain the amount of metal precipitation in the whole mantle; (4) quantifying wetting behavior

of metallic melt in polyphase assemblages that include ferropericlase and  $\text{CaSiO}_3$ -perovskite at low stress conditions; and (5) identifying physical mechanism separate Fe-Ni-S liquid from percolation (e.g., silicate crystal annealing) at lower mantle conditions.

## 7. Concluding Remarks

The genesis of Fe-Ni-S liquid features is a natural consequence of the solidification of an early, deep magma ocean: dynamic constraints show that trapping and retaining small amounts of Fe-Ni-S liquids are likely to occur during and following the solidification of a magma ocean. Retention of minor amounts of Fe-Ni-S liquids in silicates is compatible with current experimental constraints, particularly given uncertainties about the role of nonhydrostatic stresses. The model further suggests that small quantities of Fe-Ni-S liquids trapped at depth have limited impact on the siderophile element budget of the planet and predicts that LLSP material, if entrained within upwellings, would manifest itself as a high  ${}^3\text{He}/{}^4\text{He}$  component in magmas. Finally, Fe-Ni-S liquid enrichment in LLSPs implies that these features are primordial, long-lived, and chemically reduced and that they are our planet's only known manifestation of incomplete segregation of Fe-Ni-S liquids into Earth's core.

### Acknowledgments

We thank Cin-ty Lee and another anonymous reviewer for their constructive comments. This manuscript originated from a project group discussion at the 2014 CIDER summer program at the Kavli Institute of Theoretical Physics at the University of California at Santa Barbara. We pay tribute to Adam Dziewonski, a member of the CIDER founding team. We acknowledge the leadership of Barbara Romanowicz and all participants in the program for feedback. We thank Dan Frost for discussion. CIDER was supported by the NSF Frontiers of Earth Systems Dynamics grant EAR-1135452. L.S. was supported by the European Research Council under advanced grant 291432 "Molten Earth" (FP7/2007-2013). S.D. thanks the Marie Heim-Vögtlin program of the Swiss National Science Foundation for support through project PMPDP2\_151256. J.L. was supported by a Carnegie (Geophysical Laboratory) postdoctoral fellowship. M.M. was supported by the NSF under grant EAR-1135382. Q.W. was supported by the NSF under grant EAR-1215745. Z.Z. was supported by the NSF under grant EAR-1426772.

### References

- Alfè, D. (2005), Melting curve of  $\text{MgO}$  from first-principles simulations, *Phys. Rev. Lett.*, **94**, 23,5701.
- Andrault, D., S. Petitgirard, G. Lo Nigro, J.-L. Devidal, G. Veronesi, G. Garbarino, and M. Mezouar (2012), Solid-liquid iron partitioning in Earth's deep mantle, *Nature*, **487**, 354–357.
- Anzellini, S., A. Dewaele, M. Mezouar, P. Loubeyre, and G. Morard (2013), Melting of iron at Earth's inner core boundary based on fast X-ray diffraction, *Science*, **340**, 464–466.
- Belien, I. B., K. V. Cashman, and A. W. Rempel (2010), Gas accumulation in particle-rich suspensions and implications for bubble populations in crystal-rich magma, *Earth Planet. Sci. Lett.*, **297**, 133–140.
- Bouhifd, M. A., A. P. Jephcoat, V. S. Heber, and S. P. Kelley (2013), Helium in Earth's early core, *Nat. Geosci.*, **6**, 982–986.
- Burke, K., B. Steinberger, T. H. Torsvik, and M. A. Smethurst (2008), Plume generation zones at the margins of large low shear velocity provinces on the core–mantle boundary, *Earth Planet. Sci. Lett.*, **265**, 49–60.
- Cerantola, V., N. P. Walte, and D. C. Rubie (2015), Deformation of a crystalline olivine aggregate containing two immiscible liquids: Implications for early core–mantle differentiation, *Earth Planet. Sci. Lett.*, **417**, 67–77.
- Christensen, U. R., and A. W. Hofmann (1994), Segregation of subducted oceanic crust in the convecting mantle, *J. Geophys. Res.*, **99**, 19,867–19,884, doi:10.1029/93JB03403.
- Coltice, N., M. Moreira, J. Hernlund, and S. Labrosse (2011), Crystallization of a basal magma ocean recorded by helium and neon, *Earth Planet. Sci. Lett.*, **308**, 193–199.
- Davaille, A. (1999), Simultaneous generation of hotspots and superswells by convection in a heterogeneous planetary mantle, *Nature*, **402**, 756–760.
- Davies, D. R., S. Goes, J. H. Davies, B. S. A. Schuberth, H.-P. Bunge, and J. Ritsema (2012), Reconciling dynamic and seismic models of Earth's lower mantle: The dominant role of thermal heterogeneity, *Earth Planet. Sci. Lett.*, **353–354**, 253–269.
- Deschamps, F., L. Cobden, and P. J. Tackley (2012), The primitive nature of large low shear-wave velocity provinces, *Earth Planet. Sci. Lett.*, **349–350**, 198–208.
- Fiquet, G., A. L. Auzende, J. Siebert, A. Corgne, H. Bureau, H. Ozawa, and G. Garbarino (2010), Melting of peridotite to 140 gigapascals, *Science*, **329**, 1516–1518.
- Frost, D. J., C. Liebske, F. Langenhorst, C. A. McCammon, R. G. Trønnes, and D. C. Rubie (2004), Experimental evidence for the existence of iron-rich metal in the Earth's lower mantle, *Nature*, **428**, 409–412.
- Garnero, E. J. (2000), Heterogeneity of the lowermost mantle, *Annu. Rev. Earth Planet. Sci.*, **28**, 509–537.
- Ghanbarzadeh, S., M. A. Hesse, M. Prodanovic, and J. E. Gardner (2015), Deformation-assisted fluid percolation in rock salt, *Science*, **350**, 1069–1072.
- Hamano, K., Y. Abe, and H. Genda (2013), Emergence of two types of terrestrial planet on solidification of magma ocean, *Nature*, **497**, 607–610.
- Heber, V. S., R. A. Brooker, S. P. Kelley, and B. J. Wood (2007), Crystal–melt partitioning of noble gases (helium, neon, argon, krypton, and xenon) for olivine and clinopyroxene, *Geochim. Cosmochim. Acta*, **71**, 1041–1061.
- Hirschmann, M. (2000), Mantle solidus: Experimental constraints and the effects of peridotite composition, *Geochem. Geophys. Geosyst.*, **1**(10), 1042, doi:10.1029/2000GC000070.
- Holtzman, B. (2016), Questions on the existence, persistence, and mechanical effects of a very small melt fraction in the asthenosphere, *Geochem. Geophys. Geosyst.*, **16**, 470–484, doi:10.1002/2015GC006102.
- Huang, S., C.-T. A. Lee, and Q. Z. Yin (2014), Missing lead and high  ${}^3\text{He}/{}^4\text{He}$  in ancient sulfides associated with continental crust formation, *Sci. Rep.*, **4**, 5314.
- Ishii, M., and J. Tromp (1999), Normal-mode and free-air gravity constraints on lateral variations in velocity and density of Earth's mantle, *Science*, **285**, 1231–1236.
- Jackson, M. G., and R. W. Carlson (2011), An ancient recipe for flood-basalt genesis, *Nature*, **476**, 316–319.
- Jellinek, A. M., and M. Manga (2002), The influence of a chemical boundary layer on the fixity, spacing and lifetime of mantle plumes, *Nature*, **418**, 760–763.
- Kamada, S., E. Ohtani, H. Terasaki, T. Sakai, M. Miyahara, Y. Ohishi, and N. Hirao (2012), Melting relationships in the  $\text{Fe}-\text{Fe}_3\text{S}$  system up to the outer core conditions, *Earth Planet. Sci. Lett.*, **359–360**, 26–33.
- Labrosse, S., J. W. Hernlund, and N. Coltice (2007), A crystallizing dense magma ocean at the base of the Earth's mantle, *Nature*, **450**, 866–869.
- Lay, T., E. J. Garnero, and Q. Williams (2004), Partial melting in a thermochemical boundary layer at the base of Earth's mantle, *Phys. Earth Planet. Inter.*, **146**, 441–467.

- Lee, C.-T. A., P. Luffi, T. Höink, J. Li, R. Dasgupta, and J. Hernlund (2010), Upside-down differentiation and generation of a 'primordial' lower mantle, *Nature*, **463**, 930–933.
- Lekic, V., S. Cottaar, A. Dziewonski, and B. Romanowicz (2012), Cluster analysis of global lower mantle tomography: A new class of structure and implications for chemical heterogeneity, *Earth Planet. Sci. Lett.*, **357–358**, 68–77.
- Li, X.-D., and B. Romanowicz (1996), Global mantle shear velocity model developed using nonlinear asymptotic coupling theory, *J. Geophys. Res.*, **101**, 22,245–22,272, doi:10.1029/96JB01306.
- McNamara, A. K., and S. Zhong (2005), Thermochemical structures beneath Africa and the Pacific Ocean, *Nature*, **437**, 1136–1139.
- McNutt, M. K. (1998), Superswells, *Rev. Geophys.*, **36**, 211–244, doi:10.1029/98RG00255.
- Mukhopadhyay, S. (2012), Early differentiation and volatile accretion recorded in deep-mantle neon and xenon, *Nature*, **486**, 101–104.
- Muñoz Ramo, D., and L. Stixrude (2014), Spin crossover in  $\text{Fe}_2\text{SiO}_4$  liquid at high pressure, *Geophys. Res. Lett.*, **41**, 4512–4518, doi:10.1002/2014GL060473.
- Nakajima, M., and D. J. Stevenson (2015), Melting and mixing states of the Earth's mantle after the Moon-forming impact, *Earth Planet. Sci. Lett.*, **427**, 286–295.
- Ni, S. D., E. Tan, M. Gurnis, and D. V. Helmberger (2002), Sharp sides to the African superplume, *Science*, **296**, 1850–1852.
- Nomura, R., H. Ozawa, S. Tateno, K. Hirose, J. Hernlund, S. Muto, H. Ishii, and N. Hiraoka (2011), Spin crossover and iron-rich silicate melt in the Earth's deep mantle, *Nature*, **473**, 199–202.
- O'Neill, H. St. C. (1991), The origin of the Moon and the early history of the Earth – A chemical model. Part 2: The Earth, *Geochim. Cosmochim. Acta*, **55**, 1159–1172.
- Rickers, F., A. Fichtner, and J. Trampert (2013), The Iceland–Jan Mayen plume system and its impact on mantle dynamics in the North Atlantic region: Evidence from full-waveform inversion, *Earth Planet. Sci. Lett.*, **367**, 39–51.
- Rohrbach, A., C. Ballhaus, U. Golla-Schindler, P. Ulmer, V. S. Kamenetsky, and D. V. Kuzmin (2007), Metal saturation in the upper mantle, *Nature*, **449**, 456–458.
- Sanloup, C., B. C. Schmidt, G. Gudfinnsson, A. Dewaele, and M. Mezouar (2011), Xenon and Argon: A contrasting behaviour in olivine at depth, *Geochim. Cosmochim. Acta*, **75**, 6271–6284.
- Shaw, T. M., and P. R. Duncombe (1991), Forces between aluminum oxide grains in a silicate melt and their effect on grain boundary wetting, *J. Am. Ceram. Soc.*, **74**, 2495–2505.
- Shi, C. Y., L. Zhang, W. Yang, Y. Liu, J. Wang, Y. Meng, J. C. Andrews, and W. L. Mao (2013), Formation of an interconnected network of iron melt at Earth's lower mantle conditions, *Nat. Geosci.*, **6**, 971–975.
- Stixrude, L., and B. Karki (2005), Structure and freezing of  $\text{MgSiO}_3$  liquid in Earth's lower mantle, *Science*, **310**, 297–299.
- Stixrude, L., N. de Koker, N. Sun, M. Mookherjee, and B. B. Karki (2009), Thermodynamics of silicate liquids in the deep Earth, *Earth Planet. Sci. Lett.*, **278**, 226–232.
- Su, W.-J., R. L. Woodward, and A. M. Dziewonski (1994), Degree 12 model of shear velocity heterogeneity in the mantle, *J. Geophys. Res.*, **99**, 6945–6980, doi:10.1029/93JB03408.
- Torsvik, T. H., K. Burke, B. Steinberger, S. J. Webb, and L. D. Ashwal (2010), Diamonds sampled by plumes from the core–mantle boundary, *Nature*, **466**, 352–355.
- Usui, Y., and T. Tsuchiya (2010), Ab initio two-phase molecular dynamics on the melting curve of  $\text{SiO}_2$ , *J. Earth Sci.*, **21**, 801–810.
- Walte, N. P., D. C. Rubie, P. D. Bons, and D. J. Frost (2011), Deformation of a crystalline aggregate with a small percentage of high-dihedral-angle liquid: Implications for core–mantle differentiation during planetary formation, *Earth Planet. Sci. Lett.*, **305**, 124–134.
- Wasyljenko, L. E., M. B. Baker, A. J. R. Kent, and E. M. Stolper (2003), Near-solidus melting of the shallow upper mantle: Partial melting experiments on depleted peridotite, *J. Petrol.*, **44**, 1163–1191.
- Williams, Q., and E. Garnero (1996), Seismic evidence for partial melt at the base of Earth's mantle, *Science*, **273**, 1528–1530.

## Erratum

In the originally published version of this article, text was inadvertently omitted from section 4 of the main article and from text S5 of the supporting information. These omissions have since been corrected, and this version may be considered the authoritative version of record.

In the second paragraph of section 4, "decrease of solubility" has been corrected to read "decrease of sulfur solubility."

In the first paragraph of text S5 in the supporting information, "Fe solubility" has been corrected to read "sulfur solubility."



## IMMUNOLOGY

**Infection history matters**

People's responses to infections vary; for instance, seasonal influenza viruses kill only a fraction of the people they infect. Environmental factors such as age, health status, and even one's microbiota can influence outcomes, and now Reese *et al.* report that infection history may matter too. The authors found that both basal and vaccine-induced immune responses differed between barrier-raised mice, which are largely protected from infections, and mice sequentially infected with viruses that cause chronic infections, influenza virus, and a parasitic worm. Moreover, the gene signatures of these sequentially infected mice more closely resembled those of pet store-raised mice as compared to laboratory-raised mice and of adult blood as compared to fetal cord blood. Sequential microbial exposures of laboratory mice may therefore better model the complexity of human immunity. — KLM

*Cell Host Microbe* **19**, 713 (2016).

Previous infections may influence vaccine responses.

by four enzymes and seven accessory proteins. The accessory proteins help position the DNA for the enzymatic reactions. The excision structure also provided insights into how the integrative complex probably functions. — VV

*eLife* **5**, e14313 (2016).

## CANCER GENETICS

**Genotyping to identify cancer risk**

Certain genetic variants can increase a person's risk of developing cancer. For breast cancer, the link between *BRCA1/2* variants and increased cancer risk is well established; however, the risk conferred by other breast cancer-associated genetic variants is not as well understood. To gain more insight, Li *et al.* combined family history with 24 previously identified cancer-associated single-nucleotide variants (excluding the *BRCA1/2* genes) to develop a breast cancer risk score. Applying these risk scores prospectively to 2599 women revealed that this method was more accurate than familial history alone in determining the risk of developing breast cancer. — LMZ

*Genet. Med.* **10**:1038/gim.2016.2016.43 (2016).

organelles thus provide the cell with solvent properties that can modulate the behavior of the molecules they absorb. — GR

*Nat. Chem.* **10**:1038/NCHEM.2519 (2016).

## QUANTUM PHOTONICS

**Interchip quantum connectivity**

Optical circuits based on the fabrication of waveguides in silica have the proven capacity to transport single photons from one part of an optical chip to another. Quantum-enhanced sensing and communication applications will require the single photons and the generated quantum states of several interacting single photons to be transported between separate chips. However, the delicate nature of the quantum states has made such interconnectivity difficult to achieve. Using grating couplers on each chip and connecting them with a single-mode fiber, Wang *et al.* demonstrate the ability to generate an entangled state on one chip and transfer it to another. Such a coupling and transfer of quantum states will be crucial for developing advanced quantum-based technologies. — ISO

*Optica* **3**, 407 (2016).

## CELL BIOLOGY

**Remodeling DNA by phases**

The cell contains a number of organelles that lack membranes. Their interiors, composed of the disordered regions of proteins, probably form a mesh-like hydrogel, which behaves as a distinct solvent phase inside the cell. Nott *et al.* created model membraneless organelles in culture. These organelles destabilized double-stranded nucleic acids and preferentially bound single-stranded (ss) DNA and RNA, especially structured ssDNA or ssRNA, favoring compact oligonucleotide structures over extended ones. The interiors of membraneless

## GEOPHYSICS

**Managing metal the core left behind**

At the very base of Earth's rocky mantle lie two distinct regions called large low shear wave velocity provinces (LLSVPs). Zhang *et al.* suggest a very old origin for the LLSVPs by tying their formation to Earth's 4.5 billion years ago. Tiny amounts of metallic melt trapped at the base of the mantle during this process could explain the enigmatic properties of LLSVPs. Their model also provides a way for large-scale mantle heterogeneities to persist for billions of years. — BG

*Geophys. Rev. Lett.* **10**:1002/2016GL068560 (2016).

3                   **Primordial metallic melt in the deep mantle**

4       **Authors:** Zhou Zhang<sup>1</sup>, Susannah M. Dorfman<sup>2</sup>, Jabrane Labidi<sup>3</sup>, Shuai Zhang<sup>4</sup>, Mingming Li<sup>5</sup>,

5                   Michael Manga<sup>4</sup>, Lars Stixrude<sup>6</sup>, William F. McDonough<sup>7</sup> & Quentin Williams<sup>8</sup>

6       **Affiliations:**

7       1. Department of Earth Sciences, University of Minnesota, Minneapolis, MN 55414, USA.

8       2. Department of Earth and Environmental Sciences, Michigan State University, East Lansing,

9                   MI 48824, USA.

10      3. Geophysical Laboratory, Carnegie Institute of Washington, Washington DC 20015, USA.

11      4. Department of Earth and Planetary Science, University of California, Berkeley, California

12                   94720, USA.

13      5. School of Earth and Space Exploration, Arizona State University, Tempe, Arizona 85287,

14                   USA.

15      6. Department of Earth Sciences, University College London, London, WC1E 6BT, UK.

16      7. Department of Geology, University of Maryland, College Park, Maryland 20742-4211, USA.

17      8. Department of Earth and Planetary Sciences, University of California, Santa Cruz, California

18                   95064, USA.

19

20 **Contents of this file**

21 Text S1 to S12

22 Figure S1

23 Table S1

24

25

26 **Introduction**

27 The supporting information section includes five main components:

28

29       1) Supplementary text S1-S3 explaining the details of the calculation of geophysical  
30 properties.

31

32       2) Supplementary text S4-S10 explaining the details of the Fe-Ni-S liquid  
33 composition, and the dynamic process of Fe-Ni-S liquid generation and trapping during Magma  
34 Ocean crystallization.

35

36       4) Supplementary text S11-S12 showing a comparison of our model with previous  
37 models and proposing future work to test our model.

38

39       5) One supporting table S1 for the parameters and values used in the Magma Ocean  
40 cooling rate and scale calculation. One supporting figure for the evolution of the mean droplet  
41 radius as a function of time.

42

43

44

45

46

47

48

49

50

51

52

53

54

55

56

57

58

59

60

61

62

63

64 **Text S1) Elasticity of two-phase aggregates**

65 The S-wave velocity is controlled by the geometry of the melt inclusions, with films of melt  
66 having a markedly larger effect than spherical melt inclusions (Figure 1). The calculations for the  
67 elasticity changes produced by different textures of iron-rich melt are calculated from equations  
68 for the elasticity of two-phase aggregates presented by Watt et al. [1976] and Walsh [1969]: the  
69 general algorithm is the same as that used in Williams and Garnero [1996]. These depend on the  
70 respective bulk and shear moduli of the matrix and inclusion phase, the volume percentage of the  
71 inclusion phase, and its geometry. The bulk and shear moduli of the matrix are assumed to be  
72 those of the deep mantle, as derived from PREM [Dziewonski and Anderson, 1981]; the bulk  
73 modulus of the molten iron-rich alloy will depend on its composition, and hence is not well-  
74 constrained, while the shear modulus of the iron-rich melt is zero. As the outer core and deep  
75 mantle have bulk moduli within 1.5% of one another at the core-mantle boundary [Dziewonski  
76 and Anderson, 1981], we assume that the bulk moduli of the Fe-Ni-S liquid and silicate matrix  
77 are identical: the results are not strongly sensitive to the absolute value of the bulk modulus of  
78 the iron-rich alloy.

79

80 **Text S2) Pressure-dependence of melting points of lower mantle components**

81 Figure 2 shows a suite of lower mantle components and their pressure-dependent melting  
82 temperatures, including MgO [Alfè, 2005]; MgSiO<sub>3</sub> [Stixrude and Karki, 2005]; SiO<sub>2</sub> [Usui and  
83 Tsuchiya (2010); Pyrolite: Fiquet et al. (2010); Fe: Anzellini (2013); Fe-S eutectic: Kamada et  
84 al., 2012]; mantle geotherm [Stixrude et al., 2009]. CMB stands for core-mantle boundary. We  
85 suggest the metallic melt is a Fe-rich phase that likely lies within the Fe-Ni-S system (for details  
86 see supporting information text S5). The solidus of the Fe-Ni-S phase is at a temperature similar  
87 to the Fe-S eutectic temperature. In Figure 2, the Fe-S eutectic temperature is shown to be lower  
88 than the mantle geotherm throughout the mantle. The liquidus temperature of the Fe-Ni-S phase  
89 is between Fe-S and pure Fe metal, which depends on the composition of these Fe-Ni-S blebs at  
90 lower mantle pressures. Therefore, this Fe-Ni-S phase is suggested to be the molten phase;  
91 however, we do not preclude that other light alloying components could be present as well (e.g.,  
92 Si, C or O)—any additional components will further lower the melting temperature.

93

94 **Text S3) Temperature effects on the physical properties of LLSVPs**

95 For a given amount of iron alloy, higher temperatures of LLSVPs relative to surrounding mantle  
96 reduce the effective density contrast while increasing differences in shear wave velocity. For  
97 instance, assuming a LLSVP that is about 500 K hotter than surroundings [Deschamps et al.,  
98 2012], density is further reduced by ~0.5% due to thermal expansion (assuming thermal  
99 expansivity of  $1 \times 10^{-5} \text{ K}^{-1}$  at the lowermost mantle [Katsura et al., 2010]; its shear velocity is  
100 further reduced by  $\delta \ln V_s \sim -1.5\%$  for  $\partial \ln V_s / \partial T = -3 \times 10^{-5}$ ) [Trampert et al., 2004]. This upper bound  
101 on density contrast is again well within current seismic bounds on the density contrast of  
102 LLSVPs [Ishii and Tromp, 1999; Masters et al., 2000].

103

104 **Text S4) Time scale for solidification of the magma ocean**

105 Assume that the magma ocean initially freezes in its middle to create an "upper" and "deeper"  
106 magma ocean. The upper ocean cools rapidly because it freezes from the bottom; any crust that  
107 forms will sink and be stirred into the convecting magma ocean [Elkins-Tanton, 2012]. Freezing  
108 time for the upper magma ocean is likely less than  $10^6$  years [Elkins-Tanton, 2008].  
109

110 The deeper magma ocean will cool much more slowly as heat loss is limited by heat removed by  
111 solid-state convection in the overlying mantle. Neglecting any heat added from the core, a  
112 magma ocean with thickness  $d$  will solidify over a time

$$113 t_s = \frac{\rho[L+C(T_l-T_s)]d}{Q}, \quad (1)$$

114 where  $Q$  is the heat flux,  $C$  the specific heat,  $L$  the latent heat, and  $T_l$  and  $T_s$  are the liquidus and  
115 solidus temperatures, respectively. Using values from Table S1, we obtain 0.7 Ga. Labrosse et al.  
116 [2007] infer similar time scales.

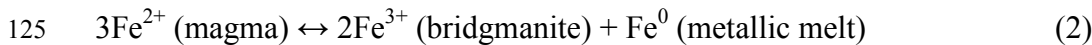
117

### 118 **Text S5) Metal precipitation in the magma ocean: amount and composition**

119

120 Fe-Ni-S liquid can exsolve from the silicate liquid as the sulfur solubility decreases in the silicate  
121 liquid as the "Hadean matte" [O'Neill, 1991]. On the other hand, Fe-Ni-S liquid could also  
122 precipitate during silicate liquid crystallization process by formation of bridgmanite.

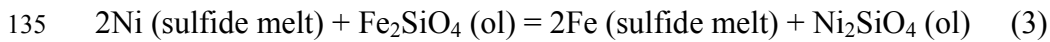
123 The oxygen fugacity at the depth of magma–metal equilibration is likely to be near 2 log units  
124 below the iron -wüstite buffer [e.g., Hirschmann, 2012], and is controlled by the reaction



126 Disproportionation of Fe in reaction (2) is driven by the incorporation of  $\text{Fe}^{3+}$  into bridgmanite  
127 [Frost et al., 2004; Frost and McCammon, 2008]. If there is insufficient  $\text{Fe}^{3+}$  in the system, then  
128 metal will precipitate. The amount of Fe metal formed will depend on how much  $\text{Fe}^{3+}$  is in the  
129 system to start, and how much  $\text{Fe}^{3+}$  is present in bridgmanite to provide charge balance at the  
130 particular conditions of interest. The latter is not well constrained.

131 Once Fe precipitates from the silicate liquid, siderophile elements such as Ni and light elements  
132 (S, C, O) will concentrate in this phase.

133 Within the upper mantle, the composition of metallic melts is controlled by the reaction



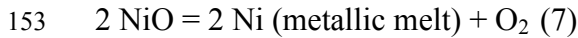
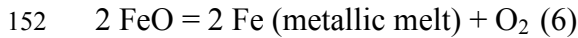
137 The Fe-Ni distribution between sulfide/alloy and olivine can be achieved through calculation of  
138 reaction (3) from experimental results. Previous studies show a Ni-rich alloy ( $\sim\text{Fe}_{0.4}\text{Ni}_{0.6}$ ) is in  
139 equilibrium with upper mantle olivine [O'Neill and Wall, 1987; Li and Agee, 1996; Holzheid  
140 and Grove, 2005; Frost and McCamoon, 2008].

141 The disproportionation reaction occurs at the Ni precipitation curve at 8 GPa in Earth's upper  
142 mantle, as shown by reactions (4) and (5), which approximate the iron and wüstite buffer [Frost  
143 and McCammon, 2008].



147 The Ni content of the metal precipitated at the Ni precipitation curve decreases with increasing  
148 pressure because the volume change for equation (5) is smaller than that of equation (4) [Frost  
149 and McCammon, 2008], which is well known from high-pressure experiments on Ni partitioning  
150 between silicate and metal [Li and Agee, 1996].

151 In the lower mantle, a similar calculation can be conducted based on the reactions



154 where the oxides are present in magnesiowustite. A similar estimate indicates that the Fe/Ni ratio  
155 of the metal droplets decreases with depth, which is further accompanied by Fe enrichment in the  
156 residual magma (Figure 4 and supporting information Text S9 for details). Therefore, the metal  
157 droplets precipitated at deeper magma ocean conditions are likely to be a Fe-rich alloy, although  
158 there is no strong constraint on their exact Ni composition.

159  
160 The sulfur partitioning coefficients between metal and silicate ( $D_{\text{metal/silicate}}$ ) are of the order of  
161 100-1000 at 15 GPa, 2500 K at oxygen fugacity near iron/wüstite -2 [Boujibar et al., 2014].  
162 Based on the preferential partitioning of S into metal, we assume that all sulfur partitions into  
163 metal droplets as the mantle crystallizes below the liquid-crystal density crossover depth. Sulfur  
164 solubility in silicate melts is ~400 µg/g in the deep upper mantle, and becomes less as pressure  
165 increases [Holzheid and Grove, 2002]. Using  $C_{\text{metal}} F_{\text{metal}} = C_{\text{silicates}}$ , where  $C_{\text{metal}}$  is the sulfur  
166 content in metal droplets,  $F_{\text{metal}}$  is the metal droplet fraction in LLSVPs (0.3-3%), and  $C_{\text{silicate}}$  is  
167 the sulfur content in the molten silicate mantle (400 µg/g), The sulfur concentration in the metal  
168 droplets is calculated to be 1-13 wt%, and the metal/sulfur atomic ratio ranges from 3-100. This  
169 may be an upper limit on the sulfur concentration in the metal droplets because: 1) sulfur  
170 solubility decreases in silicate melts with pressure; and 2) we assume the molten mantle is sulfur-  
171 saturated. In summary, the metal droplets are likely an Fe-rich Fe-Ni alloy with small amounts of  
172 sulfur (~2 wt%); the amounts of other lighter components (O, Si, C) are not well-constrained.  
173 The possible presence of other lighter alloying components (such as oxygen or carbon) within  
174 these blebs is, however, neither mandated nor precluded.

175

## 176 **Text S6) Convective velocity and length scales in the magma ocean**

177 The heat transfer and dynamics within the magma ocean are controlled by the Rayleigh number,  
178 Ra, and Taylor number, Ta:

179  $\text{Ra} = \frac{\rho g \alpha \Delta T d^3}{\mu \kappa} \quad \text{and} \quad \text{Ta} = \frac{4 \rho^2 \Omega^2 d^4}{\mu^2} ,$  (8)

180 where  $\alpha$  is the coefficient of thermal expansion,  $g$  is gravitational acceleration,  $\Omega$  is the rotation  
181 rate,  $\mu$  is the fluid viscosity,  $\kappa$  is the thermal diffusivity. The Taylor number is the ratio of inertial  
182 forces from rotation and viscous forces, and we approximate the relevant length scale as the  
183 depth of the magma ocean. With the numbers in Table S1, we obtain  $\text{Ta} \sim 10^{22}$ . Provided Ra is  
184 not less than  $10^{16}$ , which would be produced by  $\Delta T$  of  $10^{-8}$  K, rotation does not affect the heat  
185 flux  $Q$  [Solomatov, 2007].

186

187 In turbulent flows, convective velocities scales as [e.g., Deardorff, 1970]

188  $u_0 \sim \left( \frac{\alpha d g Q}{\rho c} \right)^{1/3} \sim 1.6 \text{ cm/s} .$  (9)

189 There are other scalings for so-called hard turbulence, or modifications to account for the effects  
190 of rotation, but estimates of  $u_0$  will not change dramatically.

191  
192 The Kolmogorov scale, the length scale over which turbulent motions dissipate kinetic energy  
193 into heat by viscous stresses, is

194  $l_K \sim 0.6 \left( \frac{u^3}{\rho^3 u_0^3} d \right)^{1/4} \sim 1.2 \text{ m}$  (10)

195 The magnitude of velocity fluctuations over scale  $l$  is

196  $u_l \sim u_0 \left( l/d \right)^{1/3} .$  (11)

197 At the Kolmogorov scale,  $u_l \sim 2 \times 10^{-4} \text{ m/s}.$

198

### 199 **Text S7) Fate of droplets released by the downward moving solidification front**

200 Crystals that form in the cold thermal boundary layer of the magma ocean will sink and  
201 redissolve. Fe-Ni-S liquid droplets that formed on crystal surfaces will then be liberated into the  
202 silicate melt as the crystals dissolve. The fate of these droplets depends on their size. The initial  
203 size is likely a couple microns [Yoshino and Watson, 2005]. The settling speed of droplets is

204  $u_s = \frac{2(1+\lambda)\Delta\rho g a^2}{3(2+3\lambda)\mu} ,$  (12)

205 where  $\Delta\rho$  is the density difference between the droplet and its surroundings, and  $\lambda$  is the  
206 viscosity of the droplet divided by that of the surrounding melt. Using a droplet radius  $a$  of 1  
207 micron, we obtain  $u_s \sim 10^{-8} \text{ m/s}.$  This is much smaller than both the convective velocity, and  
208 velocity at the Kolmogorov scale (but still much greater than the downward velocity of the  
209 solidification front which is  $10^{-10} \text{ m/s}.$ ) For droplets to efficiently settle through the magma  
210 ocean, their radius needs to be larger by a couple orders of magnitude.

211

212 At the droplet scale we consider two mechanisms by which droplets coalesce, either by simple  
213 shear or by buoyant settling. To compute the evolution of the droplet size distribution, we use a  
214 population balance model in which we assume that the suspension is isotropic and homogeneous  
215 [Zhang et al., 1993]. We quantify the rate at which the number of droplets per unit volume of  
216 size  $k$ ,  $n_k$ , changes owing to collisions and subsequent coalescence,

217  $\frac{dn_k(t)}{dt} = \frac{1}{2} \sum_{i+j=k} J_{ij} n_i(t) n_j(t) - n_k(t) \sum_{j=1}^{\infty} J_{kj} n_j(t).$  (13)

218 The first term accounts for the creation of droplets of size  $k$  by the coalescence of smaller  
219 droplets of size  $i$  and  $j$ , and the second terms account for their loss as they coalesce with others.  
220 The collision frequency function  $J_{ij}$  is given by

221  $J_{ij} = \pi n_i n_j (u_{s_i} - u_{s_j}) (a_i + a_j)^2 E_{ij}$  (14)

222 for buoyancy-driven motion, and

223  $J_{ij} = \frac{4}{3} n_i n_j \gamma (a_i + a_j)^3 E_{ij} ,$  (15)

224 for shear, where  $u_s$  is the Stokes velocity given by equation (12),  $\gamma$  is the shear rate, and  $E_{ij}$  is the  
225 collision efficiency based on pair-wise interactions for Stokes flows. For equations (14) and (15)

we use computed coalescence probabilities from Zhang and Davis [1991] and Wang *et al.* [1994], respectively, for the limit that the droplets are much less viscous than the suspending silicate melt. The initial size distribution has a normal distribution of the volume fraction  $\phi(a)$  about a mean radius of  $a_0$ ; the standard deviation of the initial droplet radius distribution is  $0.2a_0$ , and  $\phi_0$  is the total volume fraction of droplets.

Figure S1 shows the evolution of the mean droplet radius (weighted by volume fraction) as a function of time. Time is made dimensionless by time scales  $\frac{\mu}{\Delta \rho g a_0 \phi_0}$  for the gravitational settling problem, and  $(\gamma \phi_0)^{-1}$  for simple shear flow (neglecting settling) where  $\gamma$  is the shear rate. Choosing  $\phi_0=0.01$ ,  $a_0=10^{-6}$  m, and a strain rate of  $10^{-4}$  1/s (from above), a dimensionless time of 1 corresponds to  $\sim 3 \times 10^3$  s for gravitational settling, and  $10^6$  s for simple shear. Over time scales of days to years, we thus expect droplets to grow to sizes such that their velocities approach the convective velocity. The end product of such coalescence does leave behind a small number of small droplets (Figure S1) because coalescence rates drop to zero as size differences diverge.

Coalescence does not continue indefinitely -- droplets will break if inertial forces become too large relative to interface tension forces. For this limit, Rubie *et al.* [2003] compute a maximum droplet size of  $\sim 1$  cm. Droplets may also break if turbulent pressures and stress fluctuations become too large relative to interfacial tension forces. For this limit, Deguen *et al.* [2014] estimate maximum sizes in the 0.1 mm to 1 cm range.

#### **Text S8) Separating Fe-Ni-S liquid droplets trapped between crystals**

Near the end of the magma ocean solidification, the residual silicate melt produced by solidification becomes denser than the crystals [Muñoz Ramo and Stixrude, 2014, Figure 4]. The residual bridgmanite and ferropericlase crystals are enriched in Fe compared with the bulk silicate Earth, increasing bulk moduli [Jacobsen *et al.*, 2002; Kiefer *et al.*, 2002]. In this case, metal sulfide droplets remain trapped in the solidifying magma, and are released only if they can separate from the crystals, or drain from grain boundaries. The experiments of Shi *et al.* [2013] suggest that metal melt wets  $(\text{Mg},\text{Fe})\text{SiO}_3$ - bridgmanite at high pressure, in contrast to the behavior of metals within lower pressure silicates. Nevertheless, in the experiments of Shi *et al.* [2013], 3% of the metal remained within isolated pockets with large aspect ratios. The net role of differential stresses within the diamond anvil cell in producing the observed textures is not known: non-hydrostatic effects have been identified as generating connectivity of non-wetting melts in silicates at lower pressures, with controlled strain rates [Groebner and Kohlstedt, 2006; Walte *et al.*, 2011] or other systems [Ghanbarzadeh *et al.*, 2015]. Moreover, the wetting behaviors of the other abundant lower-mantle minerals, ferropericlase and  $\text{CaSiO}_3$ -perovskite, are not known: if either of these phases is not wet by iron-rich melts, they would function as endpoints for intergranular percolative flow. Furthermore, even in  $(\text{Mg},\text{Fe})\text{SiO}_3$ - bridgmanite where Fe-Ni-S liquid may have low dihedral angles, percolation along grain boundaries can result in melt trapping along boundaries which, with subsequent annealing, can produce separation from the percolation channel. Indeed, the trapping of fluid inclusions during crystal growth in ceramic systems is commonly observed [Shaw and Duncombe, 1991]. Moreover, fluid inclusions in mantle olivines and Fe metal blebs trapped in pallasite olivine are also commonly observed.

270 Thus, wetting of a single phase in a polyphase aggregate does not preclude trapping of melt  
271 inclusions via these multiple mechanisms.

273 In the case of Fe-Ni-S liquid forming in a magma ocean, the silicate melt will wet the grain  
274 boundaries, in which case the Fe-Ni-S liquid will be trapped at discrete droplets or ganglia (large  
275 droplets with lengths greater than the solid grains). The maximum length of ganglia, computed  
276 from percolation theory and numerical simulations, is  $l_g \sim 9 b$  where  $b$  is the crystal diameter  
277 [Wilkinson, 1984]. For these ganglia to move, buoyancy stresses  $\Delta\rho g l_g$  must overcome interfacial  
278 tension stresses  $\sigma/b$ ;  $b$  must thus exceed  $\frac{1}{3} \sqrt{\sigma/\Delta\rho g} \sim 1.5$  mm. Once these ganglia start moving,  
279 they break into smaller droplets with sizes similar to the particles [Belien et al., 2010], requiring  
280 pore sizes roughly 3 times larger to keep the droplets from being trapped again. The presence of  
281 droplets trapped in pore space also has a large influence on the permeability of the pore space for  
282 the wetting silicate melt, with the relative permeability decreasing to close to zero when the  
283 droplet fraction exceeds about 8% of the pore volume [Datta et al., 2014].  
284

### 285 **Text S9) Magma ocean density crossover**

286 We assume a magma ocean that extends to the core-mantle boundary and which begins to  
287 crystallize from the middle. We further assume: (1) (pseudo-) congruent melting of metasilicate  
288 composition, i.e.,  $\frac{Mg+Fe}{Si} = 1$  for both the liquid and crystals; (2) iron partitioning between liquid  
289 and solid has a constant partition coefficient  $= \frac{X_C*(1-X_L)}{X_L*(1-X_C)}$ , where  $X = \frac{Fe}{Fe+Mg}$  and subscripts C  
290 and L refer to crystal and liquid, respectively; (3) fractional crystallization.  
291

292 Density of the crystals are computed with HeFESTo [Stixrude and Lithgow-Bertelloni, 2011].  
293 Density of the liquid is computed following Muñoz Ramo and Stixrude [2014]. Two different  
294 pressures (136 and 100 GPa) and partition coefficients values were explored:  $K=0.4$  [Andrault et  
295 al., 2012], and  $K=0.05$  [Nomura et al., 2011].  
296

### 297 **Text S10) Elemental consistencies and noble gases**

298 The 1% Fe-Ni-S liquid within a silicate/oxide matrix could potentially cause geochemical  
299 anomalies. The estimated concentration of highly siderophile elements (e.g., platinum group  
300 elements) is in the range of  $10^0\text{-}10^1$  µg/g in the Fe-Ni-S liquid, similar to their concentration in  
301 the Earth's core [McDonough, 2003]. As the hotspot lava source might entrain  $10^{-2}$  to  $10^{-4}$  of  
302 LLSVP material, and the Fe-Ni-S liquid may comprise  $10^{-2}$  of LLSVPs, the Fe-Ni-S liquid PGE  
303 contribution to the lava is of the order of  $10^{-6}\text{-}10^{-3}$  µg/g in hotspot lavas. Compared with the PGE  
304 abundance in bulk silicate mantle,  $10^{-3}$  µg/g [McDonough and Sun, 1995], and basalts,  $10^{-1}\text{-}10^{-2}$   
305 µg/g [Lorand et al. 2008], the Fe-Ni-S liquid is not expected to create resolvable PGE anomalies.  
306 As PGEs might be depleted in the residual magma ocean due to dropping out of metal during the  
307 early stage magma ocean, the Fe-Ni-S liquid could be even further depleted in PGEs.

308 A similar calculation can be done for Ni, which has a concentration of  $\sim 10^5$  µg/g in the Fe-Ni-S  
309 liquid. The Ni contribution from Fe-Ni-S liquid to the hotspot lava is in the order  $10^{-1}\text{-}10^1$  µg/g,  
310 which is within the variation of Ni contents in mantle olivines ( $10^2$  µg/g) [Herzberg et al., 2013].  
311

312 The effects on elements like Fe and other chalcophile elements are less than for PGE's and Ni  
313 because the concentration contrasts between Fe-Ni-S liquid and ambient mantle are significantly  
314 less.

315  
316 We do not expect a W isotopic signature from the trapped Fe-Ni-S liquid. Assuming the  
317 formation of the iron droplets occurred at the time the core formed, the droplets would have a  
318 core composition in terms of W isotopes, -200 ppm relative to the ambient mantle. Direct  
319 addition of this core-like material to the OIB source, accounting for 1% of the plume material,  
320 would produce only a -2 ppm W isotope anomaly in the OIB source relative to the ambient  
321 mantle. The resolving power is presently around 2-5 ppm. A more realistic scenario in which the  
322 droplets are formed much later than the core-mantle equilibrium event would produce smaller W  
323 isotope anomalies. Because the Hf/W radionuclide system is extinct after ~90 Ma, the process  
324 that we envision would not produce any W isotope variations.  
325

326 The density of a metal-enriched LLSVP offers a physically consistent way to produce and  
327 preserve a primordial reservoir. Present-day hotspot volcanism could sample a fraction of this  
328 reservoir, leading to their primordial noble gas enrichments. Despite being the most studied  
329 noble gas, little is known about helium partitioning between silicate solids/silicate melt or silicate  
330 solids/metallic melt under the relevant lower mantle pressures and temperatures. In principle,  
331 both Fe-Ni-S liquid and its adjacent silicate crystals are potential candidates as noble gas carriers,  
332 depending on their noble gas solubilities (Fig. S2). Under crustal and upper mantle conditions,  
333 experiments have determined the helium partitioning coefficients of silicate solids/silicate liquids  
334 ( $\sim 10^{-5}$ ) and silicate liquid/metal ( $10^2$ - $10^3$ ), suggesting the highly incompatible behavior of helium  
335 in silicate solids [Heber et al., 2007; Bouhifd et al., 2013]. Similar results were found for heavier  
336 noble gases [Heber et al., 2007]. Once the silicate melt has crystallized in the magma ocean, the  
337 Fe-Ni-S liquid would be the only liquid phase in the system. Following the compatible behavior  
338 of noble gases in liquid over solids, it is possible that the Fe-Ni-S liquid could host as much  
339 noble gases as their incompatible behavior allows. In a similar approach, the noble gases were  
340 suggested to be quantitatively stored in sulfide melts when present, over silicate crystals, in the  
341 upper mantle [Huang et al., 2014]. We note that if noble gases were to have higher silicate  
342 solid/liquid partition coefficients at high pressure, as is the case for Xe [Sanloup et al. 2011],  
343 they could be stored in silicate phases rather than in Fe-Ni-S liquids (Fig S2). In this scenario,  
344 the droplet occurrence would only have acted as a physical mechanism to isolate the LLSVP  
345 from mantle convection (through a density increase), but not as the host of the noble gases  
346 (especially Xe). In both cases, however, the occurrence of the metallic droplets sets the  
347 geological context for allowing a preservation of the primordial noble gas signatures. In this  
348 scenario, the Fe-Ni-S liquids and/or silicates isolated from the rest of the convecting mantle  
349 within the LLSVPs, and hence retaining primordial elemental signatures, could generate hot spot  
350  $^3\text{He}/^4\text{He}$  compositions [Coltice et al., 2011].  
351

### 352 **Text S11) Comparison with the dense silicate solid model**

353 Compared with the model of dense silicate crystallization from the magma ocean [Labrosse et al.,  
354 2007] the Fe-Ni-S liquid model provides a better explanation for seismological observations and  
355 noble gases measurements. 20% iron content in  $\text{MgSiO}_3$  decreases the shear modulus of  $\text{MgSiO}_3$   
356 solids by ~5-15%, whereas the density increases by ~5-10% [Zhang et al., 2015]. Such a large  
357 density anomaly would not permit large relief on the LLSVPs, where the density contrast is

unlikely to exceed 2% [Ishii and Tromp 1999]. Furthermore, Deschamps et al. [2012] obtain the closest match to seismic observations with ~3% iron enrichment and 18%  $(\text{Mg}, \text{Fe})\text{SiO}_3$  enrichment. The principal challenge, which they fully recognized, “concerns the origin of such reservoirs.” The issue is thus that no well-defined process is known that generates such material; in contrast, our mechanism is based on the dynamics of magma ocean solidification, and requires only a single component to generate the seismic signature of LLSVPs.

Noble gas partitioning is another potential challenge for the dense silicate solid model. If noble gases are less incompatible at lower mantle conditions than at upper mantle conditions (e.g. partitioning coefficient  $\sim 10^{-2}$  between silicate solid/silicate liquid) [Stixrude et al., 2009; Coltice et al., 2011], both the dense silicate solid and Fe-Ni-S liquid material could host primordial noble gases in the dense layer. However, if noble gases are as incompatible as at upper mantle conditions (partitioning coefficients  $\sim 10^{-5}$ ) [Heber et al., 2007], dense silicate solids could not host sufficient primordial noble gases, and Fe-Ni-S liquid could be the major carrier of noble gases.

### **Text S12) Future tests of the model**

Our model is motivated by seismological and geochemical observations. Refinements of both types of observations will provide better tests of the model. In particular, our model makes a clear prediction for the relationship of Vs and density, implies higher electrical conductivity, and enhanced heat production which might be detected by geoneutrinos. The model further predicts that any hotspots that sample LLSVPs by mechanical entrainment would deliver elements such as primordial noble gases to the erupted lavas.

Laboratory experiments provide tests of some of the features built into the evolutionary model for creating LLSVPs. Needed are 1) noble gas partitioning experiments at  $\sim 100$  GPa to quantify partitioning between silicate crystals, Fe-Ni-S liquid and silicate liquid; 2) disproportionation experiments with silicate liquids with a range of composition at lower mantle pressures, temperatures and oxygen fugacities; 3) oxygen fugacity depth profile in the magma ocean; 4) identifying melt inclusion trapping processes at lower mantle conditions; 5) quantifying wetting behavior of Fe-Ni-S liquid in polyphase assemblages that include ferropericlase and  $\text{CaSiO}_3$ -perovskite at low stress conditions.

An upper mantle analogy may be relevant. A global reduction of shear velocity at  $\sim 100$  km below cratons has been proposed to be caused by the presence of 1-5% monosulfide melts at depth [Helffrich et al., 2011]. Such an abundance melt phase would generate similar geophysical features (depressed seismic velocity, elevated electrical conductivity) as a corresponding (but less abundant) Fe-Ni-S liquid entrained within LLSVPs. As geophysical observations have a much higher resolution in the lithospheric mantle than in the lower mantle, testing whether sulfide melts are present in the lithospheric mantle could shed light on the degree to which the deep Earth might similarly retain sulfide-rich melts.

401 **REFERENCES**

- 402 Andrault, D., et al. (2012), Solid–liquid iron partitioning in Earth’s deep mantle, *Nature*, 487,  
403 354–357.
- 404 Alfè, D., (2005), Melting curve of MgO from first-principles simulations, *Phys. Rev. Lett.* 94,  
405 235701.
- 406 Anzellini, S., A. Dewaele, M. Mezouar, P. Loubeyre, and G. Morard (2013), Melting of iron at  
407 Earth’s inner core boundary based on fast X-ray diffraction, *Science*, 340, 464–466.
- 408 Belien, I. B., K. V. Cashman, and A. W. Rempel (2010), Gas accumulation in particle-rich  
409 suspensions and implications for bubble populations in crystal-rich magma, *Earth Planet. Sci.  
410 Lett.* 297, 133–140.
- 411 Bouhifd, M. A., A. P. Jephcoat, V. S. Heber, and S. P. Kelley (2013), Helium in Earth's early  
412 core, *Nature Geoscience*, 6, 982-986.
- 413 Boujibar, A., et al. (2014), Metal–silicate partitioning of sulphur, new experimental and  
414 thermodynamic constraints on planetary accretion, *Earth Planet. Sci. Lett.*, 391, 42-54.
- 415 Brillo, J., and I. Egry (2005), Surface tension of nickel, copper, iron and their binary alloys, *J.  
416 Materials Sci.* 40, 2213-2216.
- 417 Datta, S. S., T. S. Ramakrishnan and D. A. Weitz (2014), Mobilization of a trapped non-wetting  
418 fluid from a three-dimensional porous medium, *Physics of Fluids*, 26, 022002.
- 419 Coltice, N., M. Moreira, J. Hernlund, and S. Labrosse (2011), Crystallization of a basal magma  
420 ocean recorded by Helium and Neon, *Earth Planet. Sci. Lett.*, 308, 193-199.
- 421 Deardorff, J. W. (1970), Convective velocity and temperature scales for the unstable planetary  
422 boundary layer and for Rayleigh convection, *J. Atmos. Sci.*, 27, 1211–1213 (1970).
- 423 Deguen, R., M. Landeau, and P. Olson (2014), Turbulent metal–silicate mixing, fragmentation,  
424 and equilibration in magma oceans, *Earth Planet. Sci. Lett.*, 391, 274–287.
- 425 Deschamps, F., L. Cobden, and P. J. Tackley, (2012), The primitive nature of large low shear-  
426 wave velocity provinces, *Earth Planet. Sci. Lett.* , 349-350, 198-208.
- 427 Dziewonski, A. M., and D. L., Anderson (1981), Preliminary reference Earth model, *Phys. Earth  
428 Planet. Inter.* 25, 297-356.
- 429 Elkins-Tanton, L. T. (2012), Magma oceans in the inner solar system. *Annu. Rev. Earth Planet.  
430 Sci.*, 40, 113–39.
- 431 Elkins-Tanton, L. T. (2008), Linked magma ocean solidification and atmospheric growth for  
432 Earth and Mars, *Earth Planet. Sci. Lett.* 271, 181–191.
- 433 Fiquet, G., et al. (2010), Melting of peridotite to 140 gigapascals, *Science*, 329, 1516-1518.
- 434 Frost, D. J., et al. (2004), Experimental evidence for the existence of iron-rich metal in the  
435 Earth’s lower mantle, *Nature*, 428, 409-412.
- 436 Frost, D. J., and C. A. McCammon (2008), The redox state of Earth’s mantle, *Annu. Rev. Earth  
437 Planet. Sci.* 36, 389–420.
- 438 Ghanbarzadeh, S., M. A. Hesse, M. Prodanovic, and J. E. Gardner (2015), Deformation-assisted  
439 fluid percolation in rock salt, *Science*, 350, 1069-1072.
- 440 Groebner, N., and D. L. Kohlstedt (2006), Deformation-induced metal melt networks in silicates:  
441 Implications for core–mantle interactions in planetary bodies, *Earth Planet. Sci. Lett.*, 245,  
442 571-580 (2006).
- 443 Heber, V. S., R. A. Brooker, S. P. Kelley, and B. J. Wood (2007), Crystal–melt partitioning of  
444 noble gases (helium, neon, argon, krypton, and xenon) for olivine and clinopyroxene,  
445 *Geochim. Cosmochim. Acta*, 71, 1041-1061.

- 446 Helffrich, G., J. -M. Kendall, J. O. S. Hammond, and M. R. Carroll (2011), Sulfide melts and  
447 long-term low seismic wavespeeds in lithospheric and asthenospheric mantle, *J. Geophys.*  
448 *Res.*, 38, L11301.
- 449 Herzberg, C. et al. Nickel and helium evidence for melt above the core–mantle boundary, *Nature*,  
450 493, 393–397 (2013).
- 451 Hirschmann, M. M. (2012), Magma ocean influence on early atmosphere mass and composition,  
452 *Earth Planet. Sci. Lett.*, 341-344, 48–57.
- 453 Holzheid, A., and T. Grove (2002), Sulfur saturation limits in silicate melts and their  
454 implications for core formation scenarios for terrestrial planets, *Am. Min.*, 87, 227-237.
- 455 Holzheid, A. and T. Grove (2005), The effect of metal composition on Fe–Ni partition behavior  
456 between olivine and FeNi-metal, FeNi-carbide, FeNi-sulfide at elevated pressure, *Chem. Geol.*,  
457 221, 227-237.
- 458 Huang, S., C. -T. A. Lee, and Q. Z. Yin (2014), Missing Lead and High  $^3\text{He}/^4\text{He}$  in ancient  
459 sulfides associated with continental crust formation, *Scientific Reports*, 4, 5314.
- 460 Ishii, M., and J. Tromp (1999), Normal-mode and Free-air gravity constraints on lateral  
461 variations in velocity and density of Earth's mantle, *Science*, 285, 1231-1236.
- 462 Jacobsen, S. D., et al. (2002), Structure and elasticity of single-crystal (Mg,Fe)O and a new  
463 method of generating shear waves for gigahertz ultrasonic interferometry, *Geophys. Res. Lett.*,  
464 107, ECV 4-1–ECV 4-14.
- 465 Kamada, S., et al. (2012) Melting relationships in the Fe–Fe<sub>3</sub>S system up to the outer core  
466 conditions, *Earth Planet. Sci. Lett.*, 359–360, 26–33.
- 467 Katsura, T., A. Yoneda, D. Yamazaki, T. Yoshino, and E. Ito (2010), Adiabatic temperature  
468 profile in the mantle, *Phys. Earth Planet. Inter.*, 183, 212-218.
- 469 Kiefer, B., L. Stixrude, and R. M. Wentzcovitch (2002), Elasticity of (Mg,Fe)SiO<sub>3</sub>-perovskite at  
470 high pressures, *Geophys. Res. Lett.*, 29, 34-1-34-4.
- 471 Labrosse, S., J. W. Hernlund, and N. Coltice, (2007), A crystallizing dense magma ocean at the  
472 base of the Earth's mantle, *Nature*, 450, 866–869.
- 473 Li, J., and C. B. Agee (1996), Geochemistry of mantle–core differentiation at high pressure,  
474 *Nature*, 381, 686-689.
- 475 Lorand, J. -P., A. Luguet, and O. Alard (2008), Platinum-Group Elements: A New Set of Key  
476 Tracers for the Earth's Interior, *Elements*, 4, 247–252.
- 477 Marrocchi, Y., A. Guillaume, and N. Estrade (2015) Multiple carriers of Q noble gases in  
478 primitive meteorites, *Geophys. Res. Lett.*, 42, 2093–2099.
- 479 Masters, G., G. Laske, H. Bolton, and A. M. Dziewonski (2000), The relative behavior of shear  
480 velocity, bulk sound speed, and compressional velocity in the mantle: Implications for  
481 chemical and thermal structure, in *Earth's Deep Interior: Mineral Physics and Tomography*  
482 *From the Atomic to the Global Scale*, *Geophys. Monogr. Ser.* 117, edited by S. Karato et al.,  
483 63–86, AGU, Washington, D. C.
- 484 McDonough, W. F. (2003), Compositional model for the Earth's core, *Treatise on Geochemistry*,  
485 2, 547-568, in *The Mantle and Core* (ed. R. W. Carlson) (eds. H. D. Holland and K. K.  
486 Turekian), Elsevier-Pergamon, Oxford.
- 487 McDonough, W. F., and S.-S. Sun (1995), The composition of the Earth, *Chem. Geol.* 120, 223-  
488 253 (1995).
- 489 Muñoz Ramo, D., and L. Stixrude (2014) Spin crossover in Fe<sub>2</sub>SiO<sub>4</sub> liquid at high pressure,  
490 *Geophys. Res. Lett.*, 41, 4512-4518.
- 491 Nomura, R., et al. (2012), Spin crossover and iron-rich silicate melt in the Earth's deep mantle,

- 492      Nature, 473, 199-202.
- 493      O'Neill, H. St. C., and V. J. Wall (1987), The Olivine—Orthopyroxene—Spinel Oxygen  
494      Geobarometer, the Nickel Precipitation Curve, and the Oxygen Fugacity of the Earth's Upper  
495      Mantle, *J. Petrol.* 28, 1169-1191.
- 496      O'Neill, H. St. C. (1991), The origin of the Moon and the early history of the Earth – A chemical  
497      model. Part 2: The Earth. *Geochim. Cosmochim. Acta*, 55, 1159-1172.
- 498      Rubie, D. C., H. J. Melosh, J. E. Reid, C. Liebske, and K. Righter (2003), Mechanisms of metal–  
499      silicate equilibration in the terrestrial magma ocean, *Earth Planet. Sci. Lett.*, 205, 239–255.
- 500      Shaw, T. M., and P. R. Duncombe (1991), Forces between aluminum oxide grains in a silicate  
501      melt and their effect on grain boundary wetting, *J. Am. Ceram. Soc.*, 74, 2495-2505.
- 502      Shi, C. Y., et al. (2013), Formation of an interconnected network of iron melt at Earth's lower  
503      mantle conditions, *Nat. Geosci.*, 6, 971-975.
- 504      Stixrude, L., N. de Koker, N. Sun, M. Mookherjee, and B. B. Karki (2009), Thermodynamics of  
505      silicate liquids in the deep Earth, *Earth Planet. Sci. Lett.*, 278, 226–232.
- 506      Stixrude, L., and B., Karki (2005), Structure and freezing of  $\text{MgSiO}_3$  liquid in Earth's lower  
507      mantle, *Science*, 310, 297-299.
- 508      Stixrude, L. and C. Lithgow-Bertelloni, (2011), Thermodynamics of mantle minerals - II. Phase  
509      equilibria, *Geophys. J. Int.*, 184, 1180–1213.
- 510      Solomatov, V. (2007), Magma oceans and primordial mantle differentiation, in *Treatise on  
511      Geophysics* 9, 91–120. Oxford: Elsevier (ed. Schubert).
- 512      Trampert, J., F. Deschamps, J. Resovsky, and D. Yuen (2004), Probabilistic tomography maps  
513      chemical heterogeneities throughout the Lower Mantle, *Science*, 306, 853-856.
- 514      Usui, Y., and T. Tsuchiya (2010) Ab initio two-phase molecular dynamics on the melting curve  
515      of  $\text{SiO}_2$ , *J. Earth Sci.*, 21, 801-810.
- 516      Walker, D. and O. Mullins, Jr (1981) Surface Tension of Natural Silicate Melts from 1200 °C  
517      and implications for melt structure, *Contrib. Min. Petrol.* 76, 455-462.
- 518      Walsh, J. B. (1969), New analysis of attenuation in partially melted rock, *J. Geophys. Res.*, 74,  
519      4333-4337.
- 520      Walte, N. P., D. C. Rubie, P. D. Bons, and D. J. Frost (2011), Deformation of a crystalline  
521      aggregate with a small percentage of high-dihedral-angle liquid: Implications for core–mantle  
522      differentiation during planetary formation, *Earth Planet. Sci. Lett.*, 305, 124-134.
- 523      Wang, H., A. Zinchenko, and R. H. Davis (1994) The collision rate of small drops in linear flow  
524      Fields, *J. Fluid Mech.*, 265, 161-188.
- 525      Watt, J. P., G. F. Davies, and R. J. O'Connell (1976), The elastic properties of composite  
526      materials, *Rev. Geophys. Space Phys.*, 14, 541-563.
- 527      Wilkinson, D. (1984), Percolation model of immiscible displacement in the presence of  
528      buoyancy forces, *Physical Review, A* 30, 520-531.
- 529      Williams, Q., and E. Garnero (1996) Seismic evidence for partial melt at the base of Earth's  
530      mantle, *Science*, 273, 1528-1530.
- 531      Yoshino, T., and E.B. Watson (2005) Growth kinetics of FeS melt in partially molten peridotite:  
532      an analog for core-forming processes, *Earth Planet. Sci. Lett.*, 235, 453–468.
- 533      Zhang, S., S. Cottaar, T. Liu, S. Stackhouse and B. Militzer (2016), High-pressure, temperature  
534      elasticity of Fe- and Al-bearing  $\text{MgSiO}_3$ : implications for the Earth's lower mantle,  
535      *Earth Planet. Sci. Lett.*, 434, 264-273.
- 536      Zhang, X., and R. H. Davis, (1991), The rate of collisions due to Brownian or gravitational  
537      motion of small drops, *J. Fluid Mech.*, 230, 479-504.

538 Zhang, X., H. Wang, and R. H. Davis (1993) Collective effects of temperature gradients and  
 539 gravity on droplet coalescence, Physics of Fluids A 5, 1602-1613.

540 Zhang, Y. and Z. Xu (1995) Atomic radii of noble gas elements in condensed phases, Am. Min.,  
 541 80, 670-675.

542  
 543  
 544  
 545 **Table S1:** Parameters and values  
 546

Parameter	Meaning	Value
$Q$	Heat flux	0.3 W/m <sup>2</sup>
$L$	Latent heat	10 <sup>6</sup> J/kg
$C$	Specific heat	10 <sup>3</sup> J/kg K
$T_l - T_s$	Liquidus-solidus temperature	200 K
$\rho$	density	5000 kg/m <sup>3</sup>
$D$	Magma ocean depth	1000 km
$G$	Gravitational acceleration	10 m/s <sup>2</sup>
$\Omega$	Rotation rate	10 <sup>-5</sup> s <sup>-1</sup>
$\alpha$	Coefficient of thermal expansion	3 × 10 <sup>5</sup> K <sup>-1</sup>
$\kappa$	Thermal diffusivity	10 <sup>-6</sup> m <sup>2</sup> /s
$\Delta\rho$	Density difference between metal droplets and silicate melt	3000 kg/m <sup>3</sup>
$\mu$	Viscosity	1 Pa·s
$\sigma$	Interfacial tension	0.6 N/m

547  
 548  
 549 **Figure S1:** Top) Increase in mean bubble radius (weighted by volume fraction), relative to the  
 550 initial bubble size as a function of dimensionless time. For buoyant droplets (solid curve as  
 551 “settling”) time is normalized by  $\frac{\mu}{\Delta\rho g a_0 \phi_0}$ ; for simple shear (dashed curve as “shear”) time is  
 552 normalize by  $(\gamma \phi_0)^{-1}$  where  $\gamma$  is the shear rate. Bottom) distribution of bubble radii at the time  
 553 that the mean radius has increased by a factor of 100. Dashed curves (“shear”) are for  
 554 coalescence by shear and the solid curves are for buoyancy-driven settling (solid curve as  
 555 “settling”).

556  
 557 **Figure S2:**

558 The partitioning coefficients of noble gases between sulfide liquid - silicate liquid and metal  
 559 liquid – silicate liquid. The partitioning coefficients are calculated from the semi-empirical  
 560 relationship with liquid macroscopic surface tension [Huang et al. 2014].

562 
$$D = \frac{C_2}{C_1} = \exp\left[\frac{-4\pi r^2 N_A}{RT} (\gamma_2 - \gamma_1)\right]$$

Parameter	Meaning	Value
$D$	partitioning coefficient	
$C_2$	noble gas solubility in metal liquid or sulfide liquid	

$C_1$	noble gas solubility in silicate liquid	
$r$	atomic radius as six-fold coordination:	Helium (1.08 Å)
	Reference [Zhang and Xu 1995]	Xenon (1.96 Å)
$N_A$	Avogadro's number.	$6.022 \times 10^{23}$
$R$	gas constant	$8.314 \text{ J K}^{-1} \text{ mol}^{-1}$
$T$	temperature	K
$\gamma$	liquid surface tension	
	sulfide liquid [Mungall and Su 2005] (1500-1600K)	0.55 N/m
	Fe-Ni metal liquid $\gamma = 1.82 + (T - 1500) \times 3.2 \times 10^{-4}$ (T=1500-2000 K) [Brillo and Egry 2005]	N/m
	Silicate liquid	N/m
	$\gamma = 1.82 + (T - 1500) \times 6 \times 10^{-5}$ (T=1500-2000 K) [Walker and Mullins 1981]	N/m

564

565 Sulfide liquid surface tension is kept constant as 0.55 N/m in the calculation's temperature range  
 566 of 1500-2000 K. In our hypothesis, the Fe-Ni-S liquid composition is between Fe-Ni alloy liquid  
 567 and sulfide liquid.

568

569

570

571

572

573

574

575

576

577

578

579

580

581

582

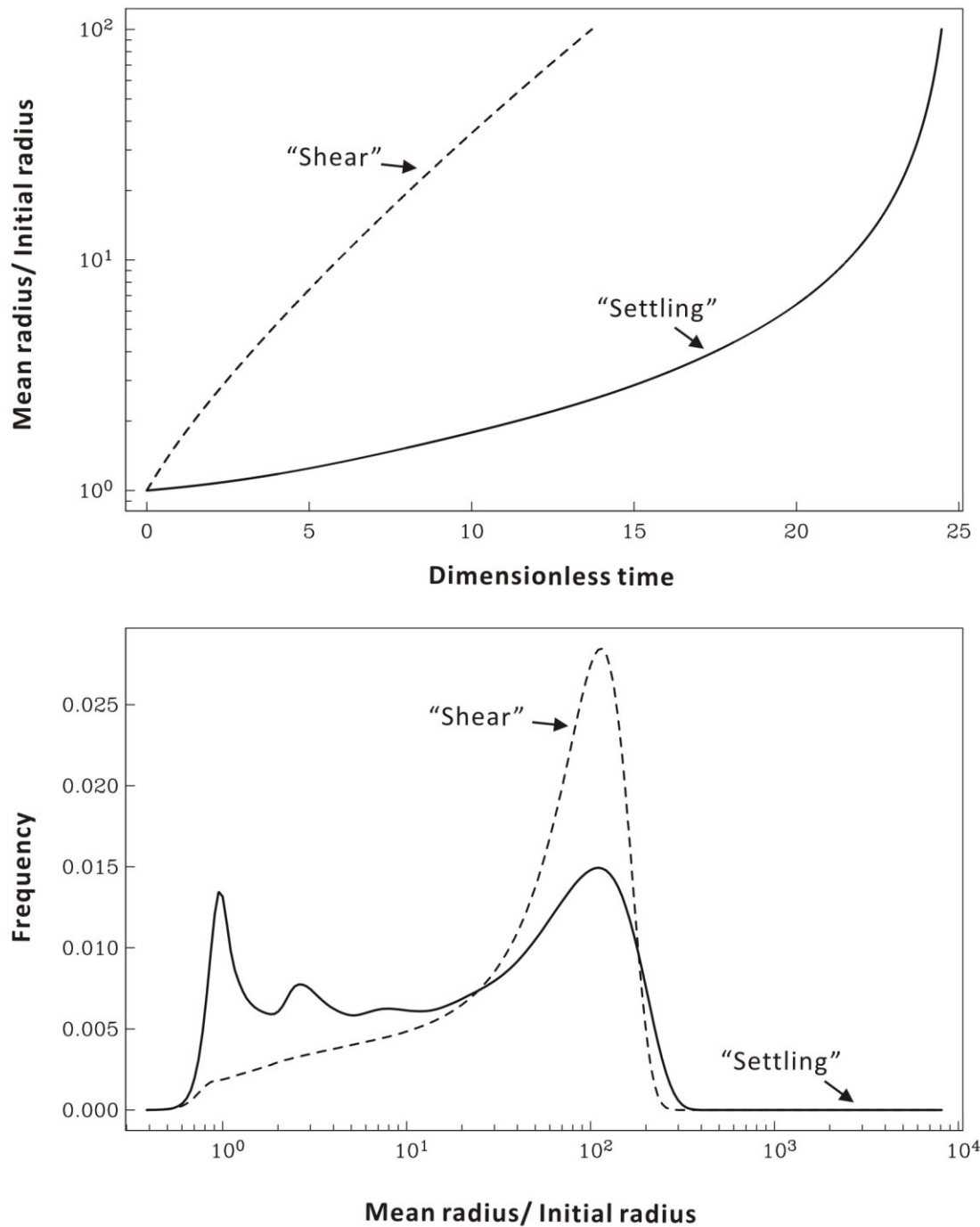
583

584

585

586

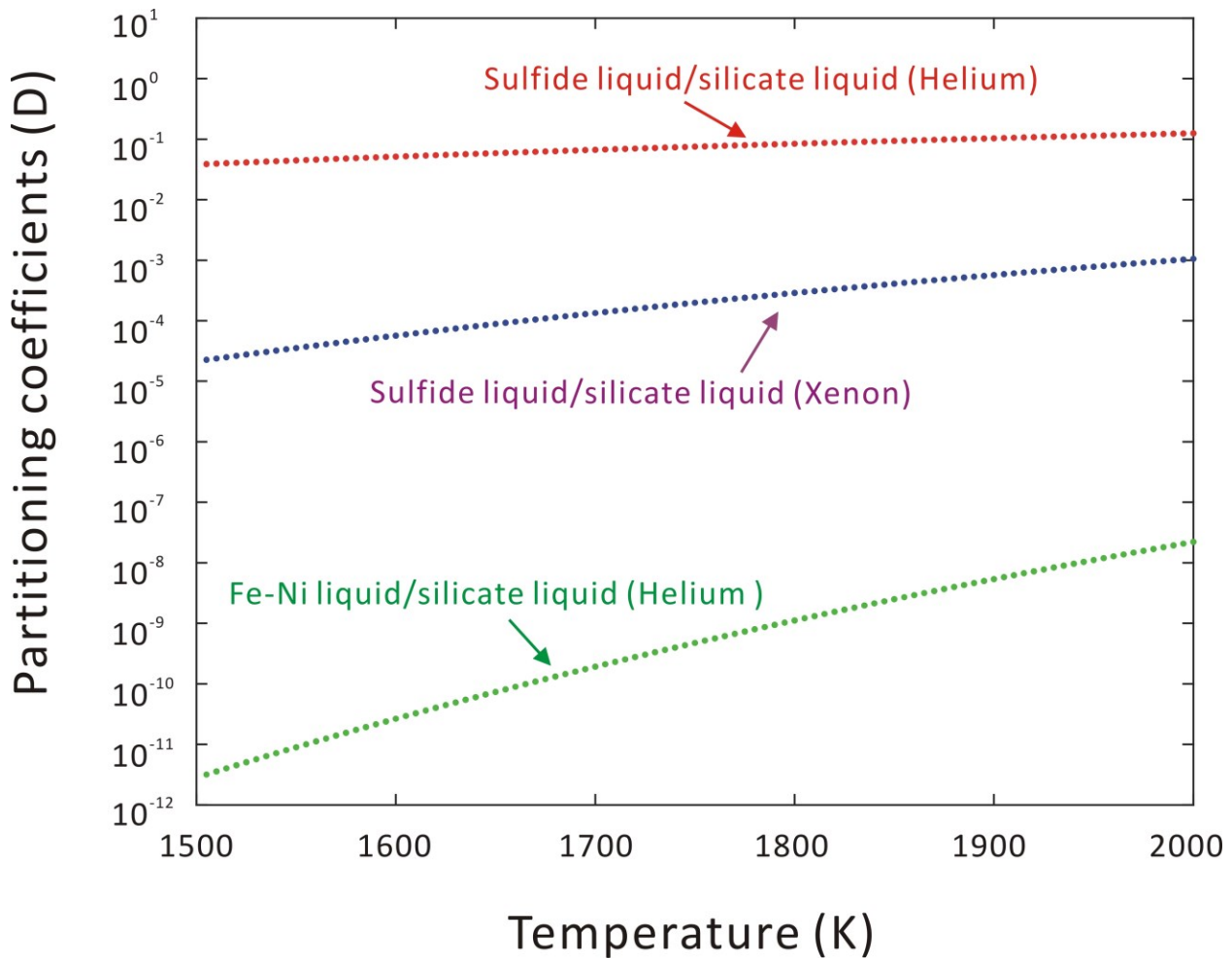
587 Fig. S1



588  
589  
590  
591  
592  
593

594  
595  
596  
597

Fig. S2



598